Numerical Studies of Near-Field Plume-Vortex Interactions

Junxiao Wu* and Suresh Menon†
School of Aerospace Engineering
Georgia Institute of Technology
Atlanta, Georgia 30332-0150

In this study, fluid mixing and chemical reactions in the near-field wake of an aircraft has been investigated. The plume-vortex regime is studied using a 3D parallel LES code. Simulations of engine plume interaction with the wing-tip vortex of B737 and B747 have been carried out and some comparisons with data have been used to demonstrate the ability of the LES method. Inclusion of detailed gas phase kinetics and simple heterogeneous processes have been carried out to evaluate the effect of turbulent mixing on the chemical processes in the plume-vortex regime. Finally, to determine the impact of temporal assumptions (often used in such flow simulations) comparison with spatial simulations are carried out. Many features of the computed flow field show reasonable agreement with experimental data. The entrainment of the engine plumes into the wing-tip vortex and also the partial detrainment of the plume were numerically captured and analyzed. The impact of fluid mechanics on the chemical process has been estimated. Results indicate that a significant difference between spatial and temporal simulation exists (especially in the predicted SO_3 concentration). This has important implications for the prediction of sulfuric acid aerosols in the wake and may partly explain the discrepancy between past numerical studies and the data. Analysis of the results also show that spatial simulation is more suitable for the near-field interaction process. For example, it was determined that detrainment (observed in the B747 contrail) was only captured using the spatial model.

1 Introduction

The wing-tip vortices shed from an aircraft's wings are known to pose a danger for aircrafts in the wake and are considered a major hazard near airports. Another consequence of the shed vortices that is perhaps less appreciated is their ability to entrain the hot exhaust of the engine during cruise flight in the upper atmosphere. The resulting species-rich and relatively long-lived contrails have been of increasing concern and a focus of research in recent years because the species entrained into the vortex wake can react with the ambient species thereby changing the local chemical balance. These studies have been motivated by the projected increase in future subsonic flights in the upper troposphere by the proposed Advanced Subsonic Transports (AST) operating in the transatlantic and Pacific rim flight corridors and by the possibility of future supersonic flights in the lower stratosphere by the High Speed Civilian Transport (HSCT).

The *near-field* region of the aircraft's wake can be divided roughly into two parts: a *plume* regime and a *plume-vortex* regime. The plume regime is identified as the initial region behind the aircraft where the engine exhaust plume grows and mixes with the ambient air. This regime is typically very short, approximately 1 sec after exhaust or around 200 m downstream of the engine exit plane. Further downstream is the plume-vortex regime where the exhaust plume is entrained into the rolled-up wing tip vortices. This regime is around $1-2$ km long and approximately 10 sec downstream of the exhaust. Due to the relatively high temperature of the engine exhaust and the species content, significant reactions can take place in the plume-vortex regime. The region downstream of the plume-vortex region is the wake region where the vortex wake breaks up due to (Crow) instability and mixes with the ambient air. This region is very large extending over 20 km and the mixing process can take many days depending upon the ambient conditions.

In the present study, the near-field region, especially the plume-vortex regime is of interest. In particular, we are interested in the chemical processes that can occur in this region due to the reaction of the emitted species with the ambient air (in particular, ozone). Key species that are of interest here are nitrogen oxides (NO_x) (generated from the oxidation of molecular nitrogen at high temperature), carbon monoxide(CO) (due to incomplete combustion), methane(CH_4), non-methane hydrocarbons(HC) and soot particles. The role of these trace species in the atmospheric photochemical and radiative processes is not very well understood. For example, the concentration of tropospheric ozone, an important greenhouse gas, is dependent on transport across tropopause and by chemical production and destruction involving reactions of NO_x, non-methane hydrocarbons, carbon monoxide,

*Graduate Research Assistant, AIAA Student Member
†Professor, AIAA Senior Member

and hydrogen oxides (HO_x). Furthermore, the radiative balance of the atmosphere can be affected by the accumulation of carbon dioxide and water (CO_2 and H_2O are the primary species in the engine exhaust) and by the aircraft-induced changes in aerosols and clouds. In addition, the combustion aerosols (soot) and the binary H_2SO_4/H_2O droplets in the plume can be efficient cloud condensation nuclei and serve as sites for heterogeneous reactions.

The ozone balance in the upper troposphere and lower stratosphere can be perturbed by an increase in NO_x and by heterogeneous reactions that take place on the surface of aerosols.[1,2] In the troposphere, NO_x acts as a catalyst to produce O_3 in reactions involving the oxidation of methane and other hydrocarbons. However, in the stratosphere, where O_3 is a barrier to ultraviolet light, NO_x catalytically destroys O_3 in reactions involving O atoms. Thus, the impact of emitted species on ozone is a function of many variables. This can complicate long-term prediction of upper atmosphere chemical balance.

A variety of models have been developed to assess the effect of aircraft flights on the atmosphere. These models generally fall into two categories: "small-scale" and "global" models. "Small-scale" models treat the near-field regime of the exhaust wake by ignoring processes that operate on larger time and space scales. Global models,[3] on the other hand, attempt to represent the large spatial scales and ignore, or represent very crudely, the small scales processes. To obtain some sort of continuity, some of the global models[3] use the engine exhaust conditions or the data at the end of the plume-vortex regime as input to their large-scale models. However, as shown recently,[4–6] the concentration of species (e.g., chemical radicals OH, HO_2 and soot) can undergo very rapid changes in the near-field. This can significantly modify the input conditions for the far field simulations. Thus, to obtain accurate prediction of the global chemical balance due to aircraft emission, the chemical processes in the plume-vortex regime is very important.

Models for the near-field regime have been developed by many researchers. The simplest model, often called the "trajectory box" model,[7,8] ignores flow transport and focuses primarily on the chemical species evolution. This type of model has been very popular since detailed chemical processes can be studied due to its computational efficiency. Models that incorporate both chemical and transport processes have also been developed. However, some approximations were employed to reduce the computational expense. For example, some models[4,9,10] used the well known SPF-II code[11] which is an efficient parabolic Navier-Stokes model. Gas phase kinetics, binary H_2SO_4-H_2O nucleation and aerosol coagulation have been studied using this model. Garnier et al.[12] used an integral model and a two-dimensional direct simulation of convection-diffusion equation to investigate the evolution of the mixing along the wake of a typical large transport aircraft. Menon and Wu[6] developed a new mixing model that included both micro- and macro-scale mixing effects and Wang and Chen[5] used a scalar probability density function model which included the large-scale mixing effect but ignored the micro-scale mixing effects. Comparison of these models was recently carried out[6] and it was demonstrated that inclusion of both macro- and micro-scale mixing results in 30% less O_3 and 15% less NO_2 depletion in the near field regime.[6]

The hydrodynamics of the plume-vortex regime is also quite complex. For example, the competition between the vortex centripetal force and gravitation buoyancy of hot plume can lead to a different final altitude of deposition of emissions.[9] This implies that evolution of the plume occurs in a highly unsteady manner. However, many of the models noted above[4,5] are steady-state models and therefore, are unable to account for the unsteady mixing effects.

To study unsteady jet-vortex interactions, unsteady methods have also been used. For example, direct numerical simulation[13] and large eddy simulation (LES) of trailing vortices[14] showed that there exists strong 3-D instability in vortex wakes with an axial deficit. The vortex instability results in vortex-stretching which may have a substantial effect on the mixing of jet plume with the ambient air. Gerz and Ehret[15] used LES to simulate the vortex roll-up process of the wake of a B-747 one second after exit. They showed that temperature, relative humidity peak at the center of the wingtip vortex, the wing boundary layer turbulence and the ambient turbulence all can affect the plume-vortex interaction process.

Unsteady simulations are computationally very expensive and therefore, most past studies employed some simplifying assumptions. For example, only limited chemical effects have been investigated so far[16] and all simulations reported so far employed periodic boundary conditions in the streamwise directions (i.e. simulated temporal evolution instead of the actual spatial evolution). Temporal approximation is truly justified only far downstream where the interaction between the jet plume and wingtip vortex has been completed. It has not yet been shown what features of the flow and the accompanying chemical processes are different and/or modified by this temporal assumption. This issue is important since it has been shown that the entrainment predicted by temporal and spatial simulations differ markedly due to the asymmetry between the high speed and the low speed sides of the shear layer.[17] The impact of this asymmetric entrainment on the chemical processes in the plume-vortex interaction regime has not been addressed so far.

This paper will address many of these issues and will attempt to quantify the impact of simulation method-

ology (i.e., spatial or temporal) on the prediction of the species distribution. Furthermore, the effect of the fluid dynamic interaction process on the chemical kinetics and on the concentration of species such as NO, SO_3 and O_3 in the plume-vortex regime will be addressed in the presence of both gas and heterogeneous kinetics.

2 Simulation Model

The simulation model used in the present study employs the LES method. In LES, scales smaller than the grid size δx are eliminated by applying an appropriately chosen low-pass filter G to the flow field variables. Any filtered field of a quantity f is given as: $\overline{f} = \int_D G(x-x')f(x')dx'$. A box filter is used since it is appropriate for finite-volume schemes.[18] Using the above definition, the original field f can be decomposed as $f = \overline{f} + f'$. For the compressible flow equations, a Favre-filter is more appropriate.[19] In this case, the Favre-filtered variable is defined as: $\tilde{f} = \frac{\overline{\rho f}}{\overline{\rho}}$. The details of the filtering operation on the Navier-Stokes equations are given in numerous publications[20,21] and therefore, avoided here for brevity. The LES equations for conservation of mass, momentum, energy and species are, respectively:

$$\frac{\partial \overline{\rho}}{\partial t} + \frac{\partial}{\partial x_i}\overline{\rho}\tilde{u}_i = 0 \tag{1}$$

$$\begin{aligned}\frac{\partial \overline{\rho}\tilde{u}_i}{\partial t} + \frac{\partial}{\partial x_j}(\overline{\rho}\tilde{u}_i\tilde{u}_j) &= -\frac{\partial \overline{p}}{\partial x_i} + \frac{\partial \tilde{\tau}_{ij}}{\partial x_j} \\ &\quad -\frac{\partial}{\partial x_j}\overline{\rho}(\widetilde{u_i u_j} - \tilde{u}_i\tilde{u}_j)\end{aligned} \tag{2}$$

$$\begin{aligned}\frac{\partial \overline{\rho}\tilde{E}}{\partial t} + \frac{\partial}{\partial x_i}(\overline{\rho}\tilde{E} + \overline{p})\tilde{u}_i &= -\frac{\partial}{\partial x_i}\rho(\widetilde{Eu_i} - \tilde{E}\tilde{u}_i) \\ &\quad -\frac{\partial}{\partial x_i}(\overline{pu_i} - \overline{p}\tilde{u}_i) \\ &\quad +\frac{\partial}{\partial x_i}(\tilde{u}_j\overline{\tau}_{ij}) \\ &\quad +\frac{\partial}{\partial x_i}(\overline{\kappa}\frac{\partial \tilde{T}}{\partial x_i})\end{aligned} \tag{3}$$

$$\begin{aligned}\frac{\partial \overline{\rho}\tilde{Y}_k}{\partial t} + \frac{\partial}{\partial x_j}(\overline{\rho}\tilde{Y}_k\tilde{u}_j) &= \tilde{w}_k - \frac{\partial}{\partial x_j}(\overline{\rho}\tilde{Y}_k\tilde{V}_j^k) \\ &\quad +\frac{\partial}{\partial x_j}(\overline{\rho Y_k u_j} - \overline{\rho}\tilde{Y}_k\tilde{u}_j)\end{aligned} \tag{4}$$

In the above equations, ρ is the density, u_i is the velocity component in ith direction, p is pressure, T is temperature and κ is the thermal conductivity. Also, Y_k, ω_k, V_j^k are, respectively, the kth species mass fraction, mass reaction rate and diffusion velocity. The kth species diffusion velocity is determined using Fick's Law of diffusion as: $V_j^k = -D\frac{\partial Y_k}{\partial x_j}/Y_k$, where D is the mixture diffusion coefficient. Also, $\overline{\tau_{ij}}$ is the viscous shear stress determined in terms of the resolved velocity gradients.

The filtered total energy $\tilde{E}$ per unit mass is defined as

$$\tilde{E} = \tilde{e} + \frac{1}{2}\tilde{u}_i\tilde{u}_i + k^{sgs} \tag{5}$$

where the subgrid kinetic energy, k^{sgs}, is defined as

$$k^{sgs} = \frac{1}{2}(\widetilde{u_i u_i} - \tilde{u}_i\tilde{u}_i) \tag{6}$$

Finally, the LES equation of the state equation is

$$\overline{p} = \overline{\rho}R\tilde{T} \tag{7}$$

In the above equation, R is the mixture gas constant given as $\sum_{k=1}^{N} Y_k R_u/W_k$ where R_u and W_k are the universal gas constant and the species molecular weight for kth species respectively, and N is the total number of species.

2.1 Subgrid Closure of the LES Equations

The above LES equations contain many terms that arise due to the filtering process and represent the effect of the unresolved subgrid fluctuation correlations on the resolved motion. Models for these unknown terms must be devised to complete the LES formulation. The key subgrid term that requires determination is the subgrid Reynolds stress term: $\tau_{ij}^{sgs} = \bar{\rho}[\widetilde{u_i u_j} - \tilde{u}_i\tilde{u}_j]$ and the subgrid enthalpy flux $H_i^{sgs} = \bar{\rho}[\widetilde{Hu_i} - \tilde{H}\tilde{u}_i]$. Here, $H = E + p/\rho$ is the stagnation enthalpy per unit mass.

A subgrid eddy viscosity closure is typically chosen for closure of the momentum and energy subgrid fluxes since the small scales primarily provide dissipation for the energy transferred from the large scales. To determine the eddy viscosity, characteristic length and velocity scales must be defined. The grid size is typically chosen as the length scale and the velocity scale in the present study is obtained by solving a transport equation for the subgrid turbulent kinetic energy, k^{sgs}. Without going into the details,[21,22] the final equation for subgrid kinetic energy is given as:

$$\begin{aligned}\frac{\partial \bar{\rho}k^{sgs}}{\partial t} + \frac{\partial}{\partial x_i}(\bar{\rho}\tilde{u}_i k^{sgs}) &= \frac{\partial}{\partial x_i}(\bar{\rho}\nu_t\frac{\partial k^{sgs}}{\partial x_i}) \\ &\quad +P_{ksgs} - D_{ksgs}\end{aligned} \tag{8}$$

In this equation, the three terms on the right-hand-side are respectively, the transport term, the production term, $P_{ksgs} = -\tau_{ij}^{sgs}\partial\tilde{u}_i/\partial x_j$ and the dissipation term $D_{ksgs} = c_\varepsilon\bar{\rho}(k^{sgs})^{3/2}/\Delta$. Here, Δ is a characteristic grid size. Once the subgrid kinetic energy is determined the subgrid stress tensor, τ_{ij}^{sgs} can be obtained as:

$$\tau_{ij}^{sgs} \approx -2\overline{\rho}\nu_t(\tilde{S}_{ij} - \frac{1}{3}\tilde{S}_{kk}\delta_{ij}) + \frac{2}{3}\overline{\rho}k^{sgs}\delta_{ij} \tag{9}$$

where $\tilde{S}_{ij} = \frac{1}{2}(\frac{\partial \tilde{u}_i}{\partial x_j} + \frac{\partial \tilde{u}_j}{\partial x_i})$ is the resolved rate-of-strain tensor and ν_t is the subgrid eddy viscosity which is approximated as $\nu_t \approx c_\nu \sqrt{k^{sgs}}\Delta$, where c_ν is a model coefficient. Similarly, the subgrid enthalpy flux term is modeled as: $\overline{\rho \tilde{H} u_i} - \overline{\rho}\tilde{H}\tilde{u}_i = -c_e \overline{\rho}\sqrt{k^{sgs}}\Delta \frac{\partial \tilde{H}}{\partial x_i}$. Here, c_ν, c_ϵ and c_e are unknown coefficients that must be specified to close the system of equations. Typically, c_e is modeled as c_ν / Pr_t where the turbulent Prandtl number as chosen as 0.9. The method used to evaluate these coefficients is described in the next section.

Closure of the species equation requires closure of the subgrid term: $\overline{\rho Y_k u_j} - \overline{\rho}\tilde{Y}_k\tilde{u}_j$. A subgrid diffusivity model (as the eddy viscosity model given above) is not considered an excellent choice since for combustion to occur species must first mix at the small scales and then, molecularly diffuse. These processes occur at the unresolved scales and therefore, a global eddy diffusivity model for the subgrid species flux that ignores the subgrid processes requires some justifications and can be used only under certain conditions. In the present study, the mixing process is dominated by the large-scale transport of the plume species into the wing-tip vortices. Furthermore, the time-scales for the subsequent chemical reactions are quite large (i.e., slow chemistry). Thus, the fast time small-scale mixing effects can be considered completed before the chemical reactions occur. For these reasons, an eddy diffusivity model for the species subgrid flux is considered a reasonable first-order approximation. With these comments in mind, the subgrid species flux is approximated as:

$$\overline{\rho Y_k u_j} - \overline{\rho}\tilde{Y}_k\tilde{u}_j = -\frac{\overline{\rho}\nu_t}{Sc^T}\frac{\partial \tilde{Y}_k}{\partial x_i} \tag{10}$$

where Sc^T is the turbulent Schmidt number set to unity for the present study.

2.2 Dynamic Evaluation of the Coefficients

The model coefficients c_ν, c_ϵ and c_e are obtained using a dynamic approach. The details of the dynamic approach has been reported elsewhere[21] and therefore, is only briefly summarized here. To obtain the model coefficients, we assume that the subgrid stresses at the grid filter level and the resolved Leonard's stress at the test filter level with a characteristic grid size $\hat{\Delta}$ (at twice the grid filter) are similar. Scale similarity between τ_{ij} and L_{ij} has been observed in some experimental data.[23] Using this similarity, the model coefficients are obtained from the following relations:

$$c_\varepsilon = \hat{\Delta}\frac{(\mu + \nu_t/\overline{\rho})d^{test}}{\langle\overline{\rho}\rangle}(k^{test})^{-3/2} \tag{11}$$

$$c_\nu = \frac{-L_{ij}D_{ij}}{2D_{ij}D_{ij}} \tag{12}$$

$$c_e = \frac{n_i d_i}{d_i d_i} \tag{13}$$

where

$$k^{test} = \frac{1}{2}\left\{\frac{\langle\overline{\rho}\tilde{u}_i\tilde{u}_i\rangle}{\langle\overline{\rho}\rangle} - \frac{\langle\overline{\rho}\tilde{u}_i\rangle}{\langle\overline{\rho}\rangle}\frac{\langle\overline{\rho}\tilde{u}_i\rangle}{\langle\overline{\rho}\rangle}\right\}$$

$$d^{test} = \left\langle\frac{\partial\tilde{u}_i}{\partial x_j}\frac{\partial\tilde{u}_j}{\partial x_i}\right\rangle - \frac{\partial}{\partial x_j}\left(\frac{\langle\overline{\rho}\tilde{u}_i\rangle}{\langle\overline{\rho}\rangle}\right)\frac{\partial}{\partial x_j}\left(\frac{\langle\overline{\rho}\tilde{u}_i\rangle}{\langle\overline{\rho}\rangle}\right)$$

The Leonard stress at the test filter level is

$$L_{ij} = \widehat{\overline{\rho}\tilde{u}_i\tilde{u}_j} - \frac{\widehat{\overline{\rho}\tilde{u}_i}\widehat{\overline{\rho}\tilde{u}_j}}{\widehat{\overline{\rho}}} - \frac{1}{3}(\widehat{\overline{\rho}\tilde{u}_k\tilde{u}_k} - \frac{\widehat{\overline{\rho}\tilde{u}_k}\widehat{\overline{\rho}\tilde{u}_k}}{\widehat{\overline{\rho}}})\delta_{ij} \tag{14}$$

and

$$D_{ij} = \hat{\Delta}\widehat{\overline{\rho}}(\frac{\widehat{\overline{\rho}\tilde{u}_l\tilde{u}_l}}{2\widehat{\overline{\rho}}} - \frac{\widehat{\overline{\rho}\tilde{u}_l}}{2\widehat{\overline{\rho}}}\frac{\widehat{\overline{\rho}\tilde{u}_l}}{\widehat{\overline{\rho}}})^{\frac{1}{2}}(\widehat{\tilde{S}_{ij}} - \frac{\widehat{\tilde{S}_{kk}}}{3}\delta_{ij}) \tag{15}$$

Finally,

$$n_i = \widehat{\overline{\rho}\tilde{H}\tilde{u}_i} - \widehat{\overline{\rho}}\widehat{\overline{H}}\widehat{\overline{u_i}} \tag{16}$$

and

$$d_i = \widehat{\overline{\rho}}(\frac{\widehat{\overline{\rho}\tilde{u}_l\tilde{u}_l}}{2\widehat{\overline{\rho}}} - \frac{\widehat{\overline{\rho}\tilde{u}_l}}{2\widehat{\overline{\rho}}}\frac{\widehat{\overline{\rho}\tilde{u}_l}}{\widehat{\overline{\rho}}})^{\frac{1}{2}}\hat{\Delta}\frac{\partial\widehat{\tilde{H}}}{\partial x_i} \tag{17}$$

The ability of this type of closure to obtain accurately the LES field for a wide range of test problems in both incompressible and compressible flows has been reported in the past.[20,21] It has also been shown in these earlier studies that predicted subgrid stresses using this model satisfies all the realizability conditions proposed by Schumann.[24] This implies that since τ_{ij}^{sgs} is a positive semi-definite tensor, the modeled term for τ_{ij}^{sgs} should also be positive semi-definite. This requirement results in the following inequalities:

$$\begin{aligned} \tau_{ii}^{sgs} &\geq 0, i \in \{1,2,3\}, \\ \left|\tau_{ij}^{sgs}\right|^2 &\leq \tau_{ii}^{sgs}\tau_{jj}^{sgs}, i,j \in \{1,2,3\}, \\ det(\tau_{ij}^{sgs}) &\geq 0. \end{aligned} \tag{18}$$

that must be satisfied. The above inequalities yield certain bounds for c_ν which must be imposed in the simulations. The present implementation of the dynamic model ensures that these requirements are satisfied during the entire simulation. Analysis shows that this criteria is automatically satisfied in over 95% of the grid points during the entire simulation.

3 Simulation Model

An explicit finite-volume scheme that is fourth order accurate in space and second-order accurate in time was used in the present study. The details of the numerical scheme has been reported elsewhere[21,22] and therefore, avoided here for brevity. The current approach is similar to the implementation described by Gamet and Estivalezes[25] except that the fluxes are modified so that a truly fourth-order accuracy in space is obtained at least on an uniform grid. The details of this implementation are given in.[22]

The present code has been parallelized using the standard Message Passing Interface (MPI) library. This allows simulation on a variety of platforms without any changes to the code. Domain decomposition method is employed whereby the computational domain is decomposed into subdomains and assigned to different processors which have an identical copy of the numerical algorithm. For the current scheme, a five point stencil is used and therefore, two rows of variables must be exchanged in either direction. Timings analysis of this code on various parallel machines (e.g., Cray T3E, SGI Origin 2000) shows that the code achieves nearly linear speedup as the number of processors is doubled. However, depending upon the total number of grid points employed there is an optimum number of processors beyond which the message passing overhead overtakes the computing time in each processor's domain.

For a $121 \times 97 \times 97$ computational grid a typical simulation (using 15 reactive species) on the Cray T3E takes around 5000 single processor hours to obtain data sufficient for statistical analysis (5 flow through time). The CPU time per time step per grid point was around 3E-6 sec on 128 processor T3E (or 3.6 sec per time step).

Two types of problems are studied in the present study. Both are in the plume-vortex regime. Figures 1a and 1b show respectively, the plume-vortex domain behind a Boeing 737 and a Boeing 747 aircraft. The primary differences are in the span, the number of engine plumes and the exhaust conditions. These two configurations were chosen primarily because there is some data available for comparison.

For slip or symmetry conditions, values are prescribed for ghost cells such that gradients normal to the face at the bounding face are zero. Periodic boundary conditions are prescribed in the streamwise direction (for the temporal simulations).

For the spatial cases, the inflow and outflow boundaries are more complicated and must be carefully implemented. We employ a method that attempts to provide reasonably accurate inflow turbulence statistics.[22,26] The inflow is critical for the spatial case since it determines the turbulence entering the computational domain. A turbulent inflow field is generated based on a prescribed energy spectrum and turbulence intensity and then superimposed on the mean field. The turbulence spectrum chosen is of the form $E(k) = Ck^4 exp(-2(k/k_p)^2)$ used by Lee *et al*,[27] where constant C is chosen as turbulence intensity level. The turbulence is divergence free and non-periodic in time. The field is stored as 3D array from which a 2-D plane is introduced at the inflow at every time step. At least 10 different arrays of $97 \times 97 \times 97$ are stored and to ensure that the inflow field is not correlated, at randomly chosen instants, the phase in the Fourier modes were randomized. Additional details of the turbulence inflow are given elsewhere.[22]

Table 1 Aircraft parameters for the near field plume-vortex calculations of B747 and B737 data.

type	wing span	maximum circulation	vortex core radius	vortex separation	engines location
B747	60m	$600m^2/s$	4m	54m	9m/18m
B737	30m	$100m^2/s$	2m	26m	5.35m

Table 2 Initial conditions for the near field plume-vortex calculations of B747.

	B747	
	Plume Condition	Ambient Condition
Temperature	500K	217K
velocity(m/sec)	247	0.0
pressure(atm)	0.17	0.17
mole fraction		
CO	$2.4\text{x}10^{-5}$	$2.0\text{x}10^{-8}$
CO_2	$3.2\text{x}10^{-2}$	$3.5\text{x}10^{-4}$
H_2	$1.0\text{x}10^{-6}$	$5.2\text{x}10^{-7}$
O_2	0.159	0.2098
OH	$1.0\text{x}10^{-5}$	$2.8\text{x}10^{-13}$
H_2O	$3.0\text{x}10^{-2}$	$4.8\text{x}10^{-6}$
N_2	0.779	0.789
NO	$4.3\text{x}10^{-5}$	$5.9\text{x}10^{-11}$
NO_2	$4.8\text{x}10^{-6}$	$4.3\text{x}10^{-10}$
N_2O_5	0.0	0.0
HNO_3	0.0	$3.3\text{x}10^{-9}$
$HONO$	0.0	0.0
SO_2	$6.9\text{x}10^{-6}$	0.0
SO_3	0.0	0.0
O_3	0.0	$2.5\text{x}10^{-7}$

The outflow boundary is non-reflecting characteristic boundary conditions.[26] The amplitudes of the outgoing waves are computed based on the interior points and the amplitude of the incoming wave is computed by specifying the background pressure. Details of this type of outflow condition is given elsewhere.

The wing-tip vortex is modeled by the Lamb-Oseen vortex[28] with an axial velocity deficit. This model has been extensively used[12–14,29–31] for earlier studies. The location, core radius, maximum circulation data of the wing-tip vortex and the engine location and exit conditions (Table 1 and 2 summarize these conditions) are chosen according to the aircraft configurations.

4 Results and Discussion

In this section, we summarize the results obtained in the present study. There are three primary objectives of this study. First, comparison with available data is carried out to demonstrate the ability of the simulation model to accurately capture the evolution of the plume-vortex regime. Second, the results obtained using temporal and spatial methods are compared to

identify what features are not predicted accurately using temporal simulations (as noted earlier, nearly all previously reported 3D studies employed periodic conditions in the streamwise direction). The final objective is to determine the impact of turbulence transport on the formation of SO_x and the destruction of ozone.

Before discussing the details of the plume-vortex interaction, the effect of different inflow turbulence on the flow field is briefly summarize. Figure 2 shows the effect of inflow turbulence on the scalar (here SO_2 concentration is used as a scalar marker) decay with increasing plume age in a B747 plume-vortex region. Three different inflow turbulence conditions are used. Two conditions employed the same energy spectrum but with 5% and 10% turbulent intensity, respectively while the third case used the same initial isotropic spectrum as other two but is introduced into the flow field after evolving for certain time with a final turbulent intensity 5%. Thus, in the third case, the inflow has evolved to a more realistic turbulent isotropic state, whereas in the first two cases the field is isotropic but is not realistic turbulence.

It can be seen that the cases with the same turbulent intensity yield almost identical results. This means that the effect of evolving of the inflow turbulent field is small at least for the global measure used here. (Note that such global measures are of interest here). However, it can be seen that turbulent intensity does have an effect on the flow field. This implies that the inflow turbulent intensity must be carefully chosen. The turbulence intensity in the vortex and jet plume varies with flight conditions such as climate, altitude and ambient flow field. A turbulent intensity between 5% and 10% is very common in the typical flight path of interest. Thus, simulations with 5% and 10% inflow turbulence may be used to quantify an upper and lower bound for the species distributions in actual flights. Interestingly, the descending vortex velocity computed from these three cases showed similar results. However, this is understandable because the descending vortex velocity is mainly determined by the overall vortex circulation and small scale turbulence exerts negligible effect on the circulation. The numerical simulation of q-vortex by Ragab and Sreedhar[29] also demonstrated this feature.

4.1 Plume-Vortex Interaction behind a Boeing 737

For quite some time under the Atmospheric Effects of Aviation Program, NASA has been conducting measurements in the wake of actual aircrafts. Some data based on ground based LIDAR measurements in the wake of a Boeing 737 is currently available for comparison. More data is expected in the near future for additional comparison.

Figure 3 shows some typical comparison of the wake LIDAR data with the present calculations. These simulations were performed using 61x101x101 grid points and using the temporal method. The initial conditions and computation domain was chosen to match the data for B737. For comparison, identical location (i.e., plume age), domain size and contour distribution is used in these figures. The chosen location is approximately $1km$ downstream of the engine exhaust (at a plume age of 5 seconds). Some interesting features can be discerned from this comparison. Note that, the numerical study enforced symmetry along the aircraft center-plane primarily to reduce the computational cost (see Figure 1a). As a result, the numerical result shows a symmetric image (obtained by mirror imaging the data) whereas the experimental data shows some asymmetry. In spite of this difference there is quite a bit of similarity in the predicted and the measured vortex structure. These features are discussed below.

First, the scale (size) and the location of the computed structure is in good agreement with data. The separation distance between the vortex pair at this demonstration location is predicted quite accurately even with symmetry boundary condition. Second, the structure of the vortex with its trailing tail (which is the jet plume as it gets entrained) is quite similar. In both the experimental data and in the present simulation, the concentration variation in the core of the vortex is very small. However, there is relatively a large variation in the outer region of the vortex. This implies that the core of the vortex has a stabilizing effect and inhibits the dilution of the passive tracer. The turbulent small-scale structures seen in the experiments are captured by the present study. On the other hand, the earlier comparison reported using the UNIWAKE method[16] did not yield this type of detail on the vortex structure and showed a scalar field that was more concentrated and coherent than the experimental data since the small scale mixing effects are neglected. The more reasonable agreement between the present LES and the data suggest a potential advantage of carrying out full 3D LES where the unsteady mixing effects are explicitly simulated.

We expect to carry out additional comparison with LIDAR data when it becomes available in the near future.

4.2 Plume-Vortex Interaction behind a Boeing 747

The LES model was also used to study the B747 wake. The key differences between the B737 and B747 are in the appropriate scales, flight conditions and the presence of two engine plumes for the B747. These simulations were carried out using both temporal and spatial methods to facilitate direct comparison. The temporal simulation captures a region of plume-vortex evolving in time which corresponds spatially (via a velocity transformation) to a location that moves (with increasing time) in the downstream direction. A grid

resolution of $121 \times 97 \times 97$ is used for both spatial and temporal simulations. For some simulations (of an extended domain) a resolution of $201 \times 111 \times 111$ was employed. The domain size (unless otherwise noted) is $24s$ in streamwise direction and $2.5s$ in other two directions. Here, s is the aircraft's semispan. Only one-half of the wake regime is simulated by employing the symmetry boundary conditions at the wake center plane.

4.2.1 Comparison with experimental data

Figure 4 shows a comparison between present spatial and temporal simulations of the passive tracer concentration on a cross-section of the plume/wake at a distance of 30 semi-spans downstream of the aircraft. The plume age is about 5 seconds. As seen earlier in Figure 3, large-scale structures are seen in both the data and the LES. The wing-tip vortex and entrainment tail of the jet plumes can be clearly seen in the present computation. Again, the concentration variation in the core of the vortex is very small even for the twin plume interaction for the B747. More, turbulent small-scale structures are seen for the B747 due to the interaction between twin plumes with the vortex.

A key difference is seen between the temporal and spatial data in the structure of the plumes as it gets entrained into the vortex. It appears that a large portion of the inboard plume is still very distinctly separated from the vortex for the spatial case whereas in the temporal case the inboard plume is also getting entrained into the vortex. The implication of this difference is discussed in the next section.

The descending vortex velocity is relatively steady within the computational range. The computed descending vortex velocity for spatial simulation and temporal simulation are 0.90 m/s and 0.86 m/s, respectively. From the data by Teske *et al.*,[16] the descending vortex velocity is around 0.93 m/s between about 15 and 40 semi-spans which is in agreement with present simulations.

Figure 5 shows the comparison of the averaged SO_2 scalar concentration decay with increasing plume age. Here, SO_2 is a marker species present initially only in the plume and therefore represents the transport and entrainment of the plume into the vortex. The current result has been normalized by the SO_2 concentration value in Teske *et al.*[16] at plume age 1 second in order to compare the dilution process between the two models. This was required since the present simulation starts with a different initial scalar concentrations when compared with Teske et al.[16] The reason is that there is no experimental data at a plume age of 1 second and the inflow setup in Teske *et al.*[16] and the present LES are not similar. The averaged passive scaler concentration is defined as the volume average of the cells which has at least one percent of the local maximum concentration. This definition was also used by Teske et al.[16]

The decrease in SO_2 concentration is mainly due to mixing with ambient air because the reaction rate for SO_2 destruction is small. The current spatial and temporal simulations are in good agreement, but there is a discrepancy between present study and the result obtained using UNIWAKE.[16] The current result shows a much larger initial decay rate than the UNIWAKE result. The experimental measurements by Arnold *et al.*[32] also showed that a lower value of SO_2 at a distance of 2km downstream of the plane than the prediction by Teske *et al.*[16] The current prediction in that region shows a better agreement with data. As Teske *et al.*[16] noted, the limitation of the turbulence model used in UNIWAKE may be contributing to this discrepancy. In the present LES with the dynamic sub-grid model the turbulent viscosity is dynamicly computed and adjusts to varying strain rate of the mean flow (i.e., different age of the plume). Thus, better comparison with the experimental data is expected and can be observed in this figure. It can also be argued that the more accurate resolution of the turbulent small-scale structures in the LES improves the prediction since turbulent diffusion plays a large role in scalar mixing. In contrast, UNIWAKE predictions ignore the small scale mixing effects. This may contribute to the under-prediction of average scalar concentration decay.

4.2.2 Detrainment of the exhaust plume

Figures 6a, 6b and 6c show respectively, three instantaneous vorticity magnitude contour plots in the x-z plane at y=0 from the spatial simulation. The two jet plumes develop almost independently before the first 4 semi-spans. After 4 semi-spans, the outboard jet plume starts to get entrained into the wing-tip vortex, and the jet plume is deflected towards the wing-tip vortex. Further downstream, the two jet plumes break up into smaller structures. This is characterized by patches of concentrated vorticity which are surrounded by flow with much lower vorticity.

The high level of intermittency seen in the flow field makes Reynolds averaged approach inapplicable since it cannot capture this effect. It can be seen that the broken portions of the outboard jet plume are deflected and entrained into the wing-tip vortex. On the contrary, due to the strong turbulent motion and relatively weak influence of the wing-tip vortex, a portion of the inboard jet plume gets *detrained* from the wing-tip vortex. Observation of contrails from widebody planes such as B747 show that there are two contrails behind the aircraft, one that is the normal vortex core contrail and another that is distinctly separated from it. As Gerz and Ehret[15] pointed out, irregular roll-up of wing-tip vortex, turbulent motion and buoyancy may result in detrainment. Gerz and Ehret[15] failed to capture detrainment in the near field by including

buoyancy effect. Also, the detrainment captured by Quackenbush *at el.*[31] was only in the far field. Present simulation suggests another reason for detrainment. This is the effect of turbulent mixing which breaks up the inboard jet plume before it gets entrained into the vortex. This in turn forms the detrained contrail as seen in Figures 6a-c.

The instantaneous NO mass fraction field corresponding to Figures 6 are shown in figures 7a, 7b and 7c, respectively. In these simulation, the species do not to have a strong effect on the fluid flow because the reactions release almost no heat. As a result, the correlation between the NO mass fraction and the vorticity magnitude is very strong. Since the reaction rate for NO species is relatively small, the NO mass fraction distribution can be used to represent the overall plume mixing process. The entrainment and detrainment of the NO species are thus similar to the vorticity field. It is worthwhile to point out that previous numerical studies[16,31] failed to capture the plume breakup and instead showed a smoothly varying plume species field. This can result in error in entrainment prediction.

Figure 8 shows a 3-D snapshot of the instantaneous vorticity magnitude isosurface with NO mass fraction contour. The sequence of the plume-vortex interaction starts with the break-up of the jet plumes. By the middle point (x=12s), the two jet plumes have broken up completely and part of the outboard jet plume starts to get entrained into the vortex. At the end of the interaction, a major part of jet plumes has been entrained into the wing-tip vortex. However, a portion of the inboard jet plume is detrained from the vortex.

The simulations by Garnier *et al.*[12] showed that the outboard jet plume scalar concentration decays faster than the inboard jet plume. They attributed this phenomenon to the wing-tip vortex effect. However, the current simulations show that both inboard and outboard plumes have almost the same decay rate even though the outboard plume is deflected toward the wing-tip vortex. When the outboard plume interacts with the wing-tip vortex, due to the shear in the flow, strong turbulence is produced. As a result, scalar mixing is enhanced and therefore, faster decay may be expected. However, when part of the plume is entrained into the core of the vortex, due to the inherent stability of the vortex core region, scalar mixing is slowed down. These two contradicting effects result in similar mixing rate for the outboard and the inboard plumes.

Another explanation for the results obtained by Garnier et al.[12] is related to the well-known over prediction by the $k-\epsilon$ turbulence model. The over prediction of the overall SO_2 decay rate by Garnier et al.[12] is also attributed to $k-\epsilon$ turbulence model.

Figures 9a and 9b show respectively, two instantaneous cross-section flow field of the vorticity magnitude contour plots at the downstream location $12s$ and $24s$ (s is the semi-span) from the temporal simulation. Figures 10a and 10b show the corresponding vorticity contour from the spatial case. There is great variety in the instantaneous cross section but these figures are very representative. At $6s$, the two jet plumes become turbulent and the interaction between the outboard jet plume and wing-tip vortex starts (not shown). At $12s$, the two jet plumes begin interact with each other and merge. However, some part of the outboard jet plume gets entrained into the wing-tip vortex. For the spatial case, at $18s$ (not shown), a large portion of the outboard jet plume is entrained into the wing-tip vortex while a major portion of the inboard jet plume stays separated.

The detrainment of the inboard plume continues as shown at x=24s and is more apparent in the spatial case than in the temporal case. Although there exist highly turbulent structures around the wing-tip vortex, the core of wing-tip vortex remains coherent and laminar. This overall observation of the plume dispersion is quite similar to the results obtained by Sykes and Henn[33] and Sykes et al.,[34] except for the addition of wing-tip vortex in present study.

Comparison of the temporal (Figs. 9) and the spatial (Figs. 10) cases show some significant differences even through the overall entrainment process is qualitatively similar. For example, in the temporal cases, the entrainment process is not very well defined in comparison to the spatial case. The detrained plume for the spatial case is also much more coherent than in the temporal case (also shown in figure 4). The inability of the temporal simulation to capture the detrainment process is due to the fact that detrainment occurs right behind the aircraft where the periodic assumption is not satisfied. This observation suggests that to capture the observed detrainment of the plume, spatial simulations are required.

4.2.3 Comparison between spatial and temporal simulations

Some differences between temporal and spatial simulations have been noted above. Namely, the spatial simulation is able to capture detrainment effects while the temporal case could not. This was attributed to the fact that in the early stages of plume-vortex interaction periodic assumption in the streamwise direction may not be appropriate. Here, to further quantify the results additional entrainment quantities are computed and compared. Figure 11 shows the detrainment ratio from the vortex core. The detrainment ratio is defined as the percentage of representative species NO outside the wing-tip vortex core which has a radius about 4m. The vortex center is located by finding the point where the minimum axial vorticity occurs. Initially, the detrainment rate is 1.0. The spatial and temporal simulations show similar trends however, the spatial simulation data has some oscillations. The os-

cillations of the spatial data could be attributed to the random wandering of wing-tip vortex which has been observed in the experiment by Devenport *et al.*[35] Thus, it would appear that spatial simulation is able to capture this random wandering effect.

As the plume begins to get entrained into the vortex core, the detrainment ratio decreases. This decrease is large in the first $12s$ and then levels off. This indicates that part of the plume has overcome the attraction of the wing-tip vortex after $12s$. This also can be seen in figure 7a, 7b and 7c where there is an apparent separation of jet plumes after $12s$. The detrainment reaches a final value of around 0.87. Therefore, about 13 percent of jet plume is entrained into the core of the wing-tip vortex.

In the vortex core, the temperature is about 8 degree higher than the ambient temperature. Note that without entrainment of the hot jet plumes, the temperature inside the wing-tip core should be a few degree lower than the ambient temperature due to the lower pressure inside the vortex core. Due to entrainment, the temperature of vortex core is increased. The several degrees' increase of temperature is critical when chemical reactions are included. This difference in temperature indicates that the entrained plume undergoes a different chemical reaction path, e.g., via the heterogeneous reactions when compared to the portion that is detrained from the vortex. The previous studies[16,31] showed only a fully entrained plume without any details of the structure inside the vortex.

It is interesting to track the different dilution processes of plume species inside and outside the vortex core since there is a lower pressure zone inside the vortex core and the fluid field is more stable inside the vortex core. It is well known that the conditions for contrail formation are very subtle and a little difference in the thermodynamics and fluid dynamics can result in widely different contrail formation. Figure 12 shows the maximum NO mass fraction inside and outside the vortex core versus downstream distance. Both spatial and temporal results are compared. Inside the vortex core, the maximum NO mass fraction is almost constant after it reaches the maximum. While, outside the vortex core the maximum NO mass fraction drops very fast in the first $12s$. The reason is that turbulent diffusion is very large outside the vortex core due to the enhanced mixing effect due to strong turbulence where jet plume breakdown occurs. On the other hand, the vortex core is relatively stable due to the swirling effect of the wing-tip vortex. After $18s$, when the turbulence begins to die down due to dissipation, the NO concentration begins to level off. Comparisons of the spatial and temporal results show that on the outside maximum NO mass fraction agrees very well. However, inside the vortex core, the temporal simulation shows a higher peak than the spatial simulation (by around 25%).

Figure 13 shows the axial variation of NO mass fraction at vortex center. Although the spatial and temporal simulations show similar trend, the spatial simulation shows a much higher mass fraction than the temporal simulation. From figure 12 and 13, one can conclude that the species distribution inside the vortex core predicted by the temporal simulation is more spread out around the core center than the prediction by the spatial simulation. This implies that the reaction rate in the temporal simulation is slower than that in the spatial simulation.

Figure 14 shows the variation of SO_3 mass fraction at vortex center with downstream distance for both spatial and temporal simulations. In the spatial simulation, SO_3 mass fraction first increases and then levels off near $24s$. On the other hand, in the temporal simulation, SO_3 mass fraction reaches a peak at around $12s$ and then decreases. There are significant difference in the magnitude of peak SO_3. The spatial data shows 10^{-8} where as the temporal data shows 10^{-11}. The wide discrepancy between temporal and spatial results has important implications for heterogeneous reactions and for H_2SO_4 aerosol formulation. This is briefly discussed below.

Note that SO_3 is produced first by the oxidization of SO_2 and then primarily removed by heterogeneous reaction on condensed soot particles. The condensation inside the core may be small due to the lower pressure. As a result, the removal rate of SO_3 is small so that SO_3 mass fraction can keep increasing downstream. The magnitude of the SO_3 mass fraction is thus determined by the rate of SO_2 oxidization reaction which is strongly affected by SO_2 mass fraction. As figures 12 and 13 suggest, the spatial data has a higher species concentration around the vortex center than the temporal data. This explains the higher SO_3 concentration in the spatial simulation. These differences between the spatial and temporal simulations show the necessity for spatial simulation.

The implication of the higher concentration of SO_3 is that it could result in an increase in the H_2SO_4 aerosol formation. Although this feature has not been included here, the present spatial LES prediction appears to partly explain the discrepancy between experimental data and earlier numerical studies. As noted earlier,[36] data suggests a 45 times higher H_2SO_4 aerosols concentration in the vortex-plume than the earlier calculations (using SPF-II type of code). The present prediction of higher SO_3 concentration obtained by doing a spatial simulation (in contrast to temporal or parabolic space marching) seems to suggest that this discrepancy may be partly due to the numerical approach. However, to confirm this we need to carry out these simulation including H_2SO_4 binary nucleation and coagulation aerosol models. This effort is underway and will be reported in the near future.

Some integrated quantities are also analyzed as fol-

lows. The mass of entrained NO into the wing-tip vortex is shown in figure 15. Temporal simulation shows a larger amount of NO is entrained than the spatial simulation. Since the relative reaction rate for NO is small, NO entrainment can be used to represent the entrainment process. The difference between the spatial and temporal simulations can be due to the axial velocity deficit of the jet plume. The deviation between the two types of simulations begins around $x = 12s$, where most of outboard engine plume is entrained into wing-tip vortex and the inboard engine plume splits into two parts. One part eventually gets entrained into the wing-tip vortex while the second part becomes detrained from the wing-tip vortex. The chemical processes that result due to the NO concentration will be different in these two regions.

Other integrated quantities of species also show significant deviation when the two simulations are compared. Figure 16 shows the mass entrainment of SO_3 into the wing-tip vortex. The result of spatial simulation shows a higher peak than the temporal simulation and shows an overall larger entrainment. This leads to the conclusion that the temporal simulation is not suitable for the early plume-vortex interaction region because there exists no periodicity in the interaction region. The discrepancy in the SO_3 concentration in the vortex is particularly bothersome as noted earlier. The increased number of aerosol measured in the wake[36] and the potential increase in the condensed sulfuric acid (due to the reaction between SO_3 and condensed water) forming on these particles have been identified as one process that could impact long term global atmosphere chemical balance.

5 Conclusions

In this study, fluid mixing and chemical reactions in the near-field wake of an aircraft has been investigated. The plume-vortex regime is studied using a 3D parallel LES code. Simulations of engine plume interaction with the wing-tip vortex of B737 and B747 have been carried out and some comparison with data have been used to demonstrate the ability of the LES method. Inclusion of detailed gas phase kinetics and simple heterogeneous processes have been carried out to evaluate the effect of turbulent mixing on the chemical processes in the plume-vortex regime. Finally, to determine the impact of temporal assumptions (often used in such flow simulations) comparison with spatial simulations were carried out.

Many features of the computed flow field show reasonable agreement with experimental data. The entrainment and detrainment of engine plumes into the wing-tip vortex were numerically captured in the spatial simulation and analyzed. The impact of fluid mechanics on the chemical process has been estimated. Results indicate that a significant difference between spatial and temporal simulation exists (especially in the predicted SO_3 concentration). This has important implication for the prediction of sulfuric acid aerosols in the wake and may partly explain the discrepancy between past numerical studies and the data. Analysis of the results also show that spatial simulation is more suitable for the near field interaction process. For example, it was determined that detrainment (observed in the B747 contrail) was only captured using the spatial model.

6 Acknowledgments

This work was supported in part by NASA Langley Research Center and the Air Force Office of Scientific Research under the Focused Research Initiative (monitored by General Electric Aircraft Engine Company, Cincinnati, Ohio). Computations were carried out at the DoD HPC center at MSRC NAVO, Stennis Space Center and ARC, Huntsville.

References

[1] Johnston, H., Kinnison, D., and Wuebbles, D., "Nitrogen oxides from high altitude aircraft: An update of potential effects on ozone," *J. Geophys. Res.*, Vol. 94, 1989, pp. 16351–16363.

[2] Beck, J., Reeves, C., de Leeuw, F., and Penkett, S., "The effect of aircraft emissions on tropospheric ozone in the northern hemisphere," *Atm. Env.*, Vol. 26, 1992, pp. 17–19.

[3] Schumann, U., "Pollution from aircraft emissions in the north Atlantic flight corridor(POLINAT)," Tech. Rep. EUR 16978 EN, Office for official publication of the European Communities Luxembourg, 1996.

[4] Brown, R., Miake-Lye, R., Anderson, M., and Kolb, C., "Aerosol dynamics in near-field aircraft plumes," *J. Geophys. Res.*, Vol. 101, 1996, pp. 22939–22953.

[5] Wang, Z. and Chen, J.-Y., "Numerical modeling of mixing and chemistry in near-field engine exhaust plumes," *J. Geophys. Res.*, Vol. 102, 1997, pp. 12871–12883.

[6] Menon, S. and Wu, J., "Effects of Micro- and Macro-scale turbulent mixing on the chemical processes in engine exhaust plumes," *J. Appl. Meteorology*, Vol. 37, 1998, In press.

[7] Karcher, B., "A trajectory box model for aircraft trailing vortices," *J. Geophys. Res.*, Vol. 100, 1995, pp. 18835–18844.

[8] Karcher, B., Peter, T., Biermann, U., and Schumann, U., "The initial composition of jet condensation trails," *J. Atm. Sci.*, Vol. 53, 1996, pp. 3066–3083.

[9] Miake-Lye, R., Martinez-Sanchez, M., Brown, R., and Kolb, C., "Plume and wake dynamics, mixing, and chemistry behind a high speed civil transport aircraft," *J. of Aircraft*, Vol. 30, 1993, pp. 467–479.

[10] Miake-Lye, R., Martinez-Sanchez, M., Brown, R., and Kolb, C., "Calculations of condensation and chemistry in an aircraft contrail," *Impact of emissions from aircraft and spacecraft upon the atmosphere*, 1994, pp. 106–112.

[11] Dash, S., Pergament, H., Wolf, D., Sinha, N., Taylor, M., and Vaughn Jr., M., *The JANNAF standardized plume flow field code version II(SPF-II), Vol. I and II, TR-CR-RD SS 90-4*, U.S. Army Missile Command, Huntsville, AL, 1990.

[12] Garnier, F., Jacquin, L., and Laverdant, A., "Engine jet entrainment in the near field of an aircraft," *Proceedings on the impact of Aircraft Emissions upon the Atmosphere.(II)*, 1996.

[13] Risso, F., Corjon, A., and Stoessel, A., "Direct numerical simulation of trailing vortices in homogeneous turbulence," *AIAA-96-0802*, 1996.

[14] Ragab, S. and Sreedhar, M., "Large-scale structures in a trailing vortex," *AIAA-94-2316*, 1994.

[15] Gerz, T. and Ehret, T., "Wake dynamics and exhaust distribution behind cruising aircraft," *AGARD-CP-584*, 1996.

[16] Teske, M., Quackenbush, T., Sykes, R., and Bilanin, A., "Long-time aircraft vortex wake predictions and plume evolution consequences," *AIAA-97-1843*, 1997.

[17] Dimotakis, P., "Two-dimensional shear laryer entrainment," *AIAA J.*, Vol. 24, 1986, pp. 1791–1796.

[18] Schumann, U., "Subgrid Scale Model for Finite Difference Simulations of turbulent Flows in Plane Channels and Annuli," *Journal of Computational Physics*, Vol. 18, 1975, pp. 376–404.

[19] Erlebacher, G., Hussaini, M. Y., Speziale, C. G., and Zang, T. A., "Toward the Large-Eddy Simulation of Compressible Turbulent Flows," *Journal of Fluid Mechanics*, Vol. 238, 1992, pp. 155–185.

[20] Kim, W.-W. and Menon, S., "A New Dynamic One-Equation Subgrid-Scale Model for Large-Eddy Simulations," *AIAA-95-0356*, 1995.

[21] Nelson, C. C. and Menon, S., "Unsteady Simulations of Compressible Spatial Mixing Layers," *AIAA-98-0786*, 1998.

[22] Nelson, C. C., *Simulations of Spatially Evolving Compressible Turbulence Using a Local Dynamic Subgrid Model*, Ph.D. thesis, Georgia Institute of Technology, Atlanta, Georgia, 1997.

[23] Liu, S., Meneveau, C., and Katz, J., "On the properties of similarity subgrid-scale models as deduced from measurements in a turbulent jet," *J. of Fluid Mech.*, Vol. 275, 1994, pp. 83–119.

[24] Schumann, U., "Realizability of Reynolds-Stress Turbulence Models," *The Physics of Fluids*, Vol. 20, No. 5, 1976, pp. 721–725.

[25] Gamet, L. and Estivalezes, J. L., "Non-reflective boundary conditions applied to jet aeroacoustics," *AIAA-95-0159*, 1995.

[26] Poinsot, T. and Lele, S., "Boundary conditions for direct simulations of compressible viscous flow," *Journal of Computational Physics*, Vol. 101, 1992, pp. 104–129.

[27] Lee, S., Lele, S., and Moin, P., "Eddy shocklets in decaying compressible turbulence," *Physics of Fluids, A*, Vol. 3, 1991, pp. 657–664.

[28] Saffman, P., "Structure of turbulent line vortices," *Phys. of Fluids*, Vol. 16, 1973, pp. 1181–1188.

[29] Ragab, S. and Sreedhar, M., "Numerical simulation of vortices with axial velocity deficits," *Phys. Fluids*, Vol. 7, 1994, pp. 549–558.

[30] Quackenbush, T., Teske, M., and Bilanin, A., "Computation of Wake/Exhaust mixing downstream of advanced transport aircraft," *AIAA-93-2944*, 1993.

[31] Quackenbush, T., Teske, M., and Bilanin, A., "Dynamics of Exhaust Plume Entrainment in Aircraft Vortex Wakes," *AIAA-96-0747*, 1996.

[32] Arnold, F., Scheneider, J., Gollinger, K., Schlager, H., Schulte, P., Hagen, D., Whitefield, P., and van Velthoven, "Observation of upper tropospheric sulfur dioxide- and acetone-pollution: potential implications for hydroxyl radical and aerosol formation," *Geophys. Res. Lett.*, Vol. 24, 1997, pp. 57–60.

[33] Sykes, R. I. and Henn, D. S., "Large-eddy simulation of concentration fluctuations in a dispersing plume," *Atm. Env.*, Vol. 26, 1992, pp. 3127–3144.

[34] Sykes, R. I., Henn, D. S., Parker, S., and Lewellen, W. S., "Large-eddy simulation of turbulent reacting plume," *Atm. Env.*, Vol. 26, 1992, pp. 2565–2574.

[35] Devenport, W., Rife, M., Liapis, S., and Follin, G., "The structure and development of a wing-tip vortex," *J. Fluid Mech.*, Vol. 312, 1996, pp. 67–106.

[36] Fahey, D., Keim, E., and Woodbridge, R. *et al.*, "*In situ* observations in aircraft exhaust plumes in the lower stratosphere at mid-latitudes," *J. Geophys. Res.*, Vol. 100, 1995, pp. 3065–3074.

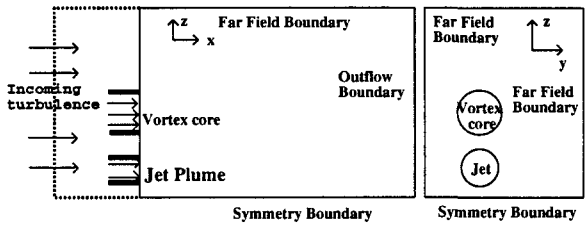

a) Computational domain for the B737 wing-tip vortex and jet plume.

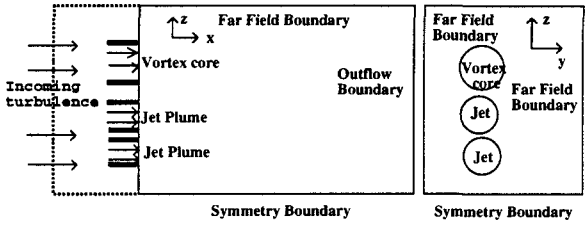

b) Computational domain for the B747 wing-tip vortex and jet plumes.

Fig. 1 Setup of the numerical simulations for the spatial LES simulations.

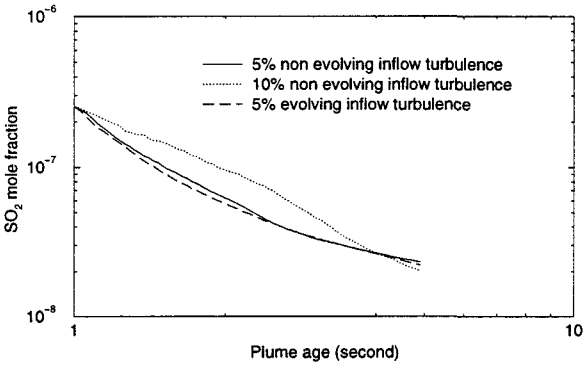

Fig. 2 Comparison of averaged SO_2 mole fraction decay for different turbulence inflow conditions.

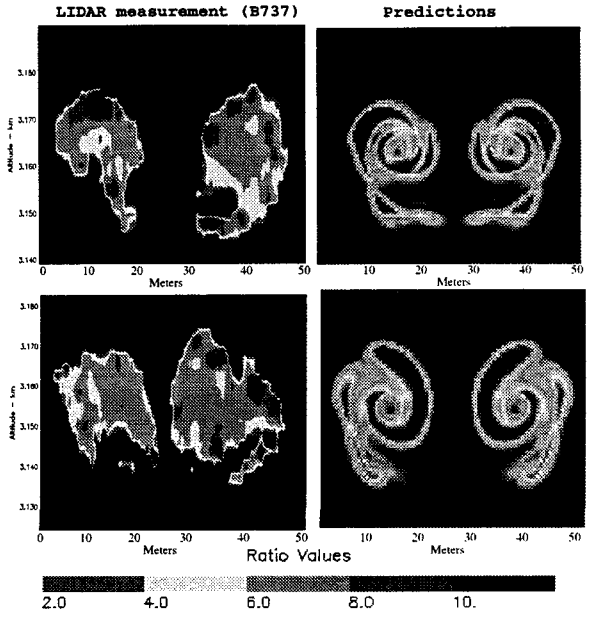

Fig. 3 Comparison of B737 scalar concentration with LIDAR measurement

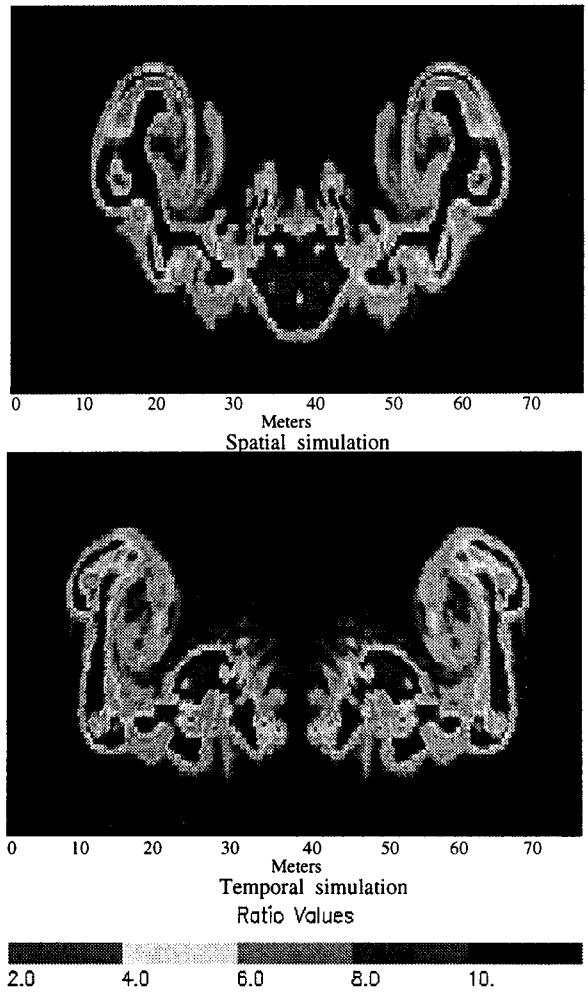

Fig. 4 Comparison of scalar concentration between spatial and temporal simulations

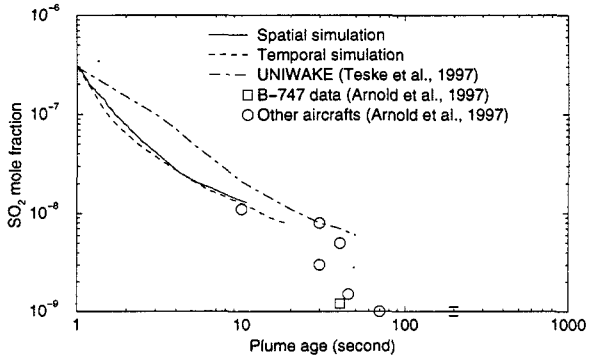

Fig. 5 Comparison of averaged SO_2 mole fraction decay with experimental data.

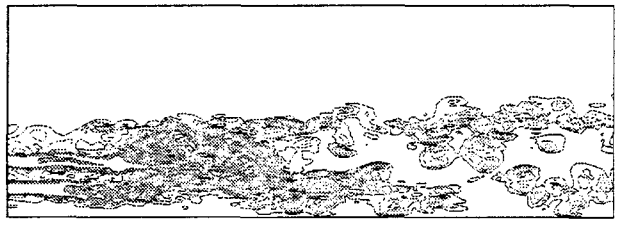

a)

b)

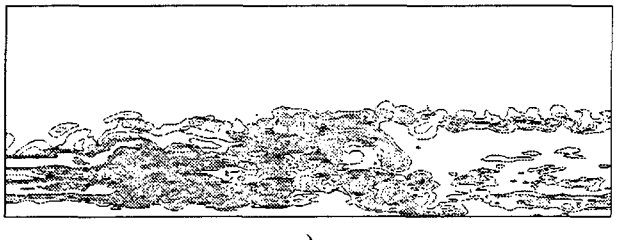

c)

Fig. 6 Instantaneous vorticity magnitude contours at different times for the spatial B747 case.

a)

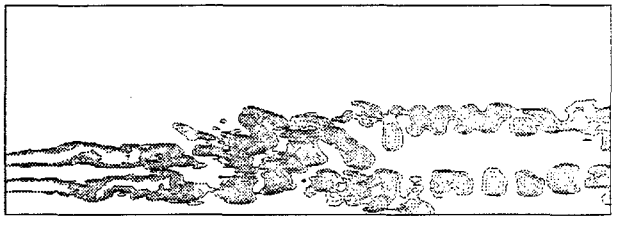

b)

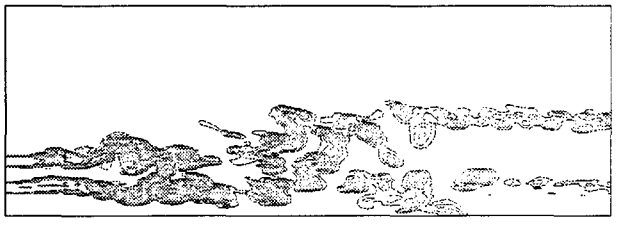

c)

Fig. 7 Instantaneous NO mass fraction contours at different times for the spatial B747 case.

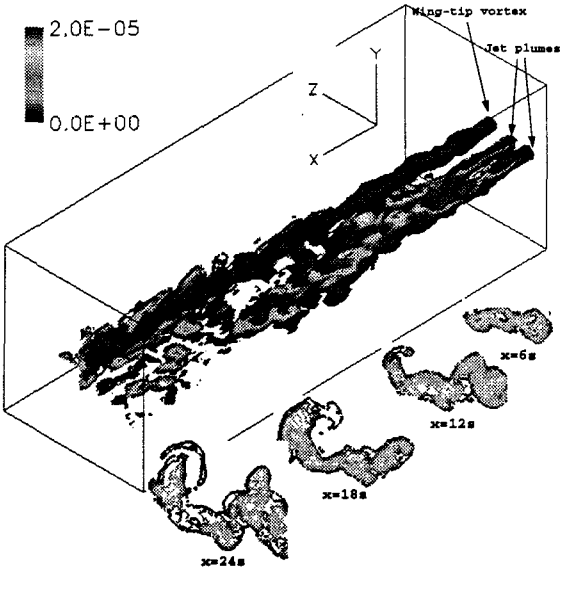

Fig. 8 3D instantaneous vorticity magnitude iso-surface for the B747 plume-vortex interaction.

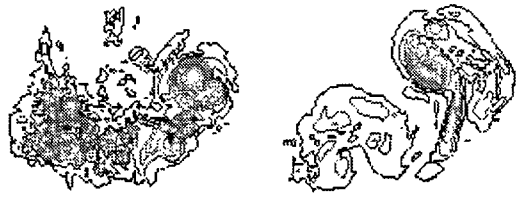

a) x=12s b) x=24s

Fig. 9 Vorticity magnitude contours at different locations in the temporal simulation.

a) x=12s b) x=24s

Fig. 10 Vorticity magnitude contours at different locations in the spatial simulation.

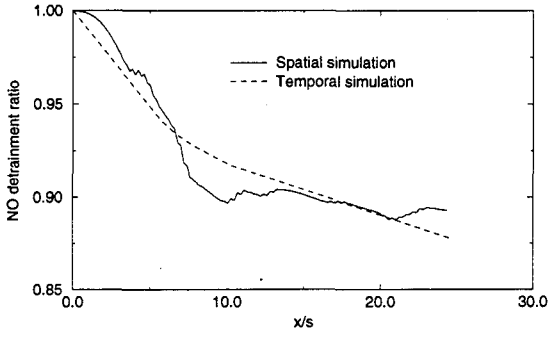

Fig. 11 Variation of the detrainment ratio of NO species with the downstream distance for B747.

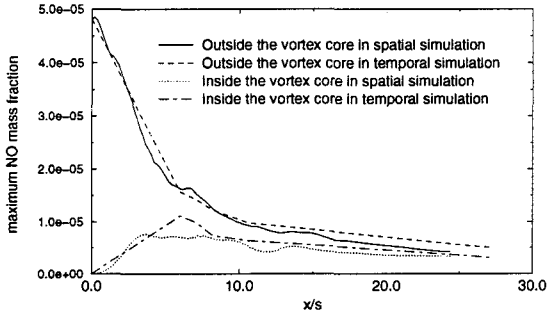

Fig. 12 Maximum NO mass fraction inside and outside the vortex core (vortex core has a radius of 4m).

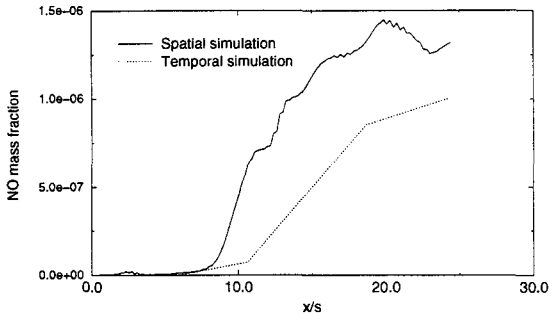

Fig. 13 NO mass fraction at the vortex core center.

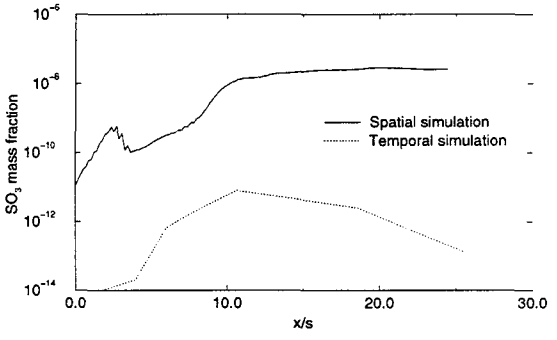

Fig. 14 SO_3 mass fraction at the vortex center.

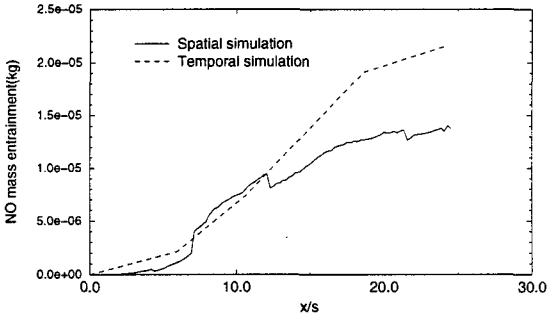

Fig. 15 NO mass entrainment into the vortex core.

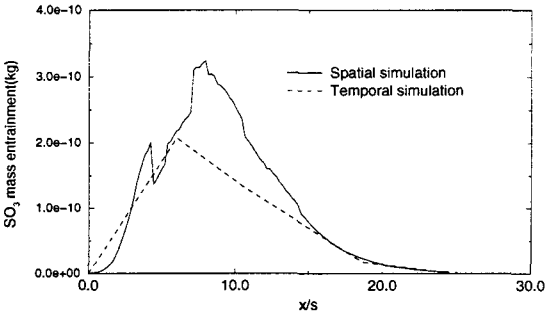

Fig. 16 SO_3 mass entrainment into the vortex core.